

Quick-scanning X-ray Absorption Fine Structure Beamline at SSRF

Yu Chen, Qian Gao, Zheng Jiang, Jiong Li*, Shuo Zhang

*lijiong@sari.ac.cn

Abstract: The layout and characteristics of the hard X-ray spectroscopy beamline (BL11B) at the Shanghai Synchrotron Radiation Facility are described herein. BL11B is a bending-magnet beamline dedicated to conventional and millisecond-scale quick-scanning X-ray absorption fine structures. It is equipped with a cylindrical collimating mirror, a double-crystal monochromator comprising Si(111) and Si(311), a channel-cut quick-scanning Si(111) monochromator, a toroidal focusing mirror, and a high harmonics rejection mirror. It can provide 5–30 keV of X-rays with a photon flux of $\sim 5 \times 10^{11}$ photons/s and an energy resolution of $\sim 1.31 \times 10^{-4}$ at 10 keV. The performance of the beamline can satisfy the demands of users in the fields of catalysis, materials, and environmental science. This paper presents an overview of the beamline design and a detailed description of its performance and capabilities.

Keywords: bending magnet beamline, X-ray absorption fine structure, quick-scanning XAFS, *in situ*, synchrotron radiation

1 INTRODUCTION

X-ray absorption fine structure (XAFS) spectroscopy is an important experimental method for synchrotron radiation facilities. It is characterized by element selectivity and local structure sensitivity, which renders it effective for investigating the local atomic and electronic structures of matter [1,2]. Owing to the rapid development of XAFS spectroscopy in recent decades, it has been widely used in cutting-edge research fields such as energy materials, catalysis, and environmental science [3,4,5,6,7,8,9,10,11,12,13]. The demand for X-ray absorption spectroscopic techniques to dynamically characterize the structures of various reactions is increasing owing to the continuously increasing effort toward scientific studies [14,15,16,17]. In particular, for some chemical reaction processes, the continuous structural evolution of materials, which involves reaction conditions and times, imposes new requirements for the development of *in situ* experimental techniques [18,19,20,21,22,23,24]. Currently, owing to the XAFS scanning-time limit of 10–30 min [25,26], *in situ* characterization is generally performed through an alternative “quasi-*in situ*” protocol, in which the external conditions are fixed at a certain position for data acquisition, followed by a change in the conditions for the next acquisition. The obtained discrete experimental data are used to predict the actual reactions. Recently, quick-scanning monochromator instruments have been successfully developed that allow rapid data acquisition in the subsecond time scale, thereby outperforming the conventional XAFS technique in terms of experimental capabilities [27,28,29,30]. The quick-scanning XAFS technique is advantageous for the real-time and dynamic monitoring of reaction processes and understanding the intrinsic

mechanisms underlying catalytic reaction processes.

In this regard, a hard X-ray absorption spectroscopy beamline, BL11B, which is dedicated to conventional and quick-scanning XAFS spectroscopy, was constructed at the Shanghai Synchrotron Radiation Facility (SSRF) [31,32,34,35]. The beamline provides a wide energy range of energy (i.e., 5–30 keV) based on a bending magnet source. The construction of the beamline was completed in December 2019, and it was officially opened to users in January 2021. As of July 2023, BL11B has delivered ~6500 h to users, and more than 300 research papers have been published in different scientific fields consequently. In the following section, we describe the optical layout and characteristics of the BL11B beamline. Additionally, the versatile experimental environments and methods as well as the first commissioning results are presented.

2 Beamline

2.1 Light source

The SSRF is a third-generation synchrotron radiation light source composed of a 3.5 GeV electron storage ring, a full energy booster, and a 150 MeV linear accelerator [32]. The electron-beam current in top-up mode is 300 mA. A bending magnet is used as the photon source for the BL11B beamline as it offers a low thermal power density, thus reducing the thermal load of the optics and improving the beamline stability. A bending magnet can provide a wide energy spectrum, which is essential for Extended X-ray Absorption Fine Structure (EXAFS). The most important specifications of the bending magnet source and BL11B beamline are summarized in Table 1.

Table 1 Specifications of bending magnet source and BL11B beamline.

Parameters of storage ring		Parameters of bending magnet	
Storage ring current (mA)	300	Magnetic field intensity (T)	1.27
Electron energy (GeV)	3.5	Critical energy (keV)	10.346
Horizontal emittance (nm·rad)	4.22	Acceptance angle (mrad ²)	1.5×0.17
Horizontal electron size (μm)	72.99	Maximum photon flux (phs/s/0.1%BW)	1.74×10 ¹³ @ 7.5 keV
Horizontal electron divergence (μrad)	118.6	Power density (W/mrad ²)	310
Vertical electron size (μm)	23.24	Total radiant power (W)	66.2
Vertical electron divergence (μrad)	1.947	Coupling ratio	1%

2.2 Beamline optics

A schematic illustration of the BL11B beamline is shown in Fig. 1. A water-cooled four-blade slit is equipped at 18.2 m from the source, which controls the maximum acceptance angle of the white beam to 1.5×0.17 mrad². The main optical elements are described as follows:

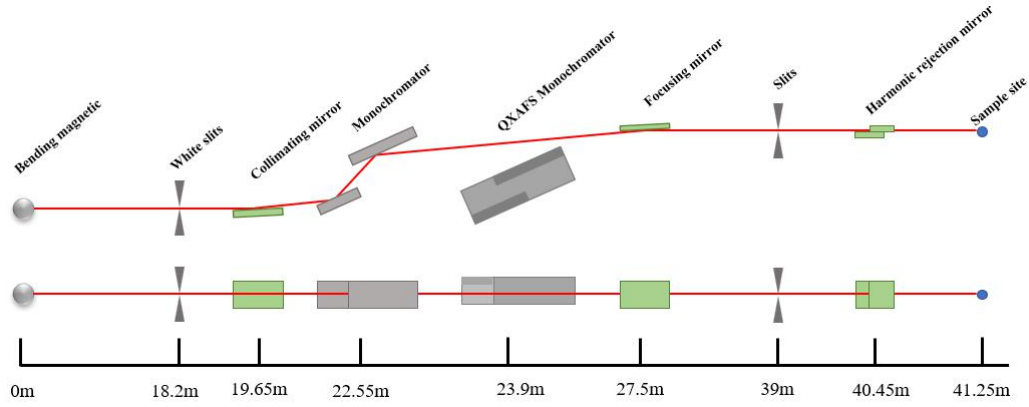


Fig. 1 Schematic illustration of optical layout of BL11B beamline.

2.2.1 Collimating mirror

The collimating mirror is the first optical element downstream of the white-beam slit. It collimates a white beam in the vertical direction to improve the energy resolution. Additionally, it can increase the vertical acceptance of the focusing mirror to increase the X-ray flux.

In BL11B, the collimating mirror is placed 19.65 m from the source. It is a cylindrical mirror bent from a plane mirror, whose tangential curvature radius can be adjusted via a bending mechanism. The mirror comprises a single-crystal Si substrate with Rh and Pt coatings, with each coating measuring 1000 mm (length) \times 40 mm (width) and featuring incident angles of 3.5 and 2.8 mrad, respectively. Owing to the two coatings, the collimating mirror affords an energy range of 5–30 keV and exhibits high reflectivity, as shown in Fig. 2. The two coatings can be switched via the horizontal translation of the mirror in the vacuum chamber. Owing to the different incident angles, the switching of the coatings will change the height of the downstream optical path. Therefore, the height of the optical elements after the collimation of the mirror must be adjusted. To reduce thermal deformation on the mirror surface, the edge of the substrate is water cooled using a copper clamp.

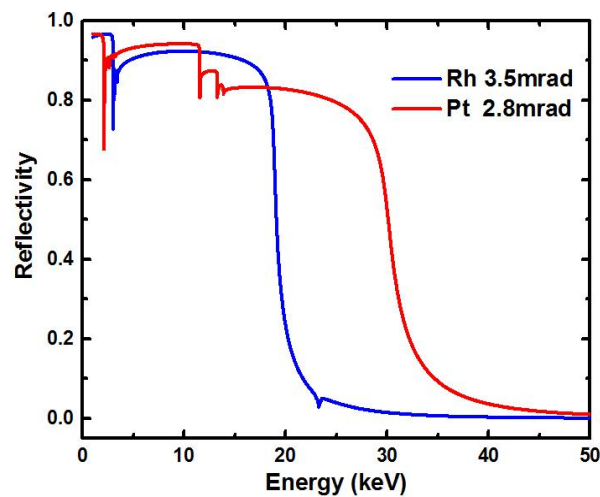


Fig. 2 Simulated reflectivity of Pt and Rh coatings of collimator mirror [33].

2.2.2 Monochromators

To satisfy the different experimental requirements, an independent double-crystal

monochromator (DCM) system and a quick-scanning monochromator system were installed sequentially at the BL11B beamline, as shown in Fig. 3.

The DCM system is located at 22.55 m from the source and comprises two sets of flat silicon crystals, i.e., Si(111) and Si(311). Si(111) crystals are suitable for intermediate energies of 5–18 keV, whereas Si(311) crystals are used for high energies of 10–30 keV. Meanwhile, Si(311) can provide a higher energy resolution to satisfy specific experimental requirements. The two crystal sets can be easily switched via a horizontal translation mechanism outside the vacuum chamber. The monochromator is designed for bounce-up operation with a fixed-exit beam offset of 20 mm. When the Bragg angle is changed, the second crystal propagates in a cascade along the Z-direction to maintain a constant 20 mm beam offset between the exit and incoming beam. A coarse stepper motor and a fine piezoactuator are used to adjust the crystal parallelism. When the two sets of crystals must be removed from the beam path, the vertical stepper motor can be operated such that the crystals shift up and down simultaneously.

The quick-scanning monochromator system is located 23.9 m from the source. It comprises a Si(111) channel-cut crystal that can encompass an energy range of 5–26.5 keV. The rapid rotation of the crystal is afforded by a direct-drive torque motor with a small oscillatory amplitude of approximately 4° . The oscillation frequency and amplitude of the crystal can be adjusted rapidly and smoothly. The drive mechanism is mounted coaxially inside a Huber 430 goniometer. The goniometer precisely aligns the center angle of the channel-cut crystal based on the selected absorption edge, and a torque motor is used to drive the oscillatory movement of the crystal during the QXAFS operation. The maximum oscillatory frequency of the channel-cut crystal is 50 Hz, which results in a time resolution of 10 ms. In addition the QXAFS operation, we can adjust the goniometer to perform a conventional step scan. For the channel-cut crystal, the two reflection surfaces of the crystal are rigidly connected, thus resulting in high stability during EXAFS scanning. Considering the relatively low heat load of the bending magnet source, both types of monochromators are water cooled.

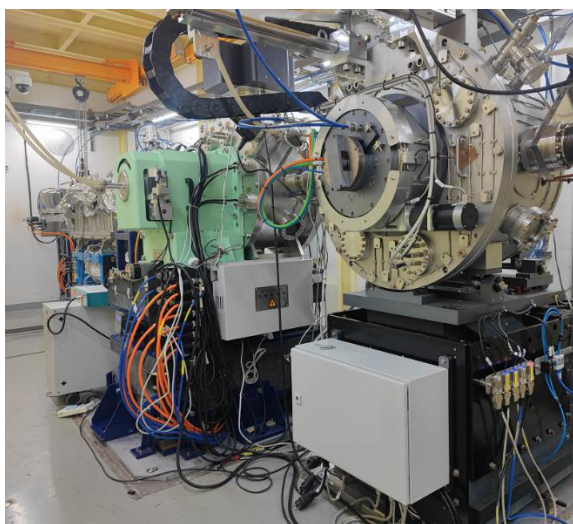


Fig. 3 Independent monochromator systems equipped at BL11B. Left: double-crystal monochromator. Right: quick-scanning channel-cut monochromator.

To satisfy the requirements of different experiments, the two sets of monochromators can be switched rapidly. When the stepping-scanning mode of the DCM is required, the channel-cut

crystal should be laid flat and shifted down to remove the crystal out of the beam path. When the quick-scanning mode of the channel-cut monochromator is required, the DCM crystals are laid flat, and the crystal spacing is increased to allow the white beam to pass through them. Additionally, the attitude and height of the focusing mirror are adjusted to optimize the spot size and photon flux at the sample position. The switching process can be completed within 30 min.

2.2.3 Toroidal focusing mirror

Following the monochromators, a toroidal focusing mirror that is bent from a cylindrical mirror is installed 27.5 m from the source. It focuses the parallel and divergent beams in the vertical and horizontal directions to the sample, respectively. The focusing mirror is shown in Fig. 4. Similar to the collimating mirror, it comprises two strips of cylindrical single-crystal Si substrates with Pt- and Rh-coated regions. The Pt-coated region features an incident angle of 2.8 mrad and a sagittal radius of 51.3 mm. The Rh-coated region features a grazing angle of 3.5 mrad and a sagittal radius of 64.2 mm. These two coating regions can be bent to the theoretical meridional radius, i.e., 19.6 and 7.9 km, respectively, via a stepper motor. The mirror is placed horizontally downward and 27.5 m from the source. To minimize the effect of aberration caused by the toroid focusing mirror, a horizontal focus ratio of 2:1 was implemented by placing the sample 13.75 m downstream of the focusing mirror.

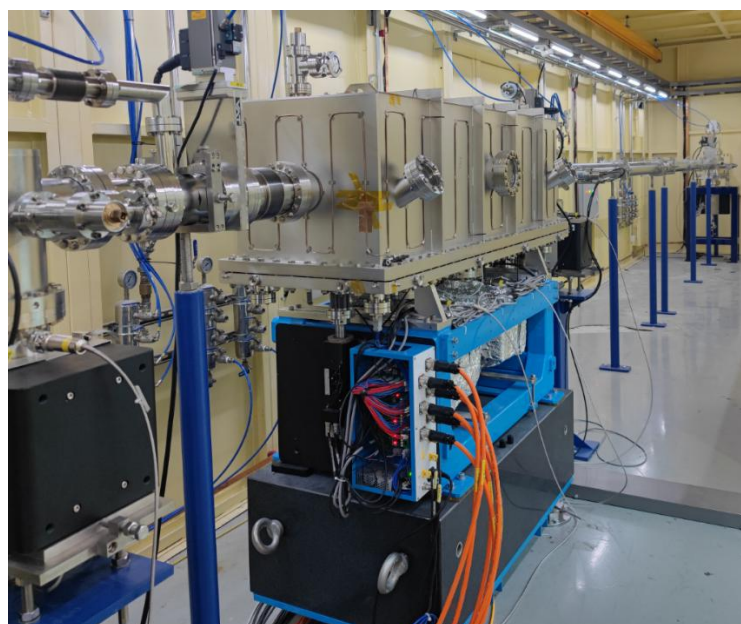


Fig. 4 Toroid focusing mirror system equipped at BL11B.

2.2.4 Harmonics-rejection mirror

To realize high-quality XAFS experiments, a specific harmonics-rejection mirror is necessitated to suppress the high-order harmonics photons of the crystal monochromators. The harmonics-rejection mirror was placed 40.45 m from the source and on an optical table in the experimental end-station, as shown in Fig. 5. It comprised two planar mirrors placed face-to-face and parallel to each other to maintain the beam direction. Moreover, it featured three reflection regions with different coatings, i.e., Si for 5–7 keV, Cr for 6.5–11 keV, and Rh for 7.5–15 keV. For energies above 15 keV, the harmonics-rejection mirror was shifted directly out of the beam path

owing to the negligible high-order harmonics. Combining the above with the collimating and focusing mirrors, the higher-harmonic contents can be reduced to less than 10^{-5} , thus satisfying the requirement of high spectral purity for XAFS experiments.

3 Experimental end-station

The experimental end-station hutch was located 37.35–45.35 m from source and measured 8 m (length) \times 3.5 m (width) \times 3.4 m (height). Various hardware communication control cabinets, instruments, and equipment were equipped in the hutch, including optical tables, detector systems, sample stages, *in situ* sample cells, and other auxiliary equipment.

The experimental platform was an optical table, on which most of the instruments were placed, as shown in Fig. 5. A harmonics-rejection mirror chamber was placed on an optical table. A high-precision four-blade slit was connected to the outlet of the harmonics-rejection mirror chamber and was used to shield stray X-rays. Furthermore, it can limit the spot size of the monochromatic X-rays on the sample, depending on the experimental requirements. After the slit, detector systems and a sample stage with vertical and horizontal translations with micrometer accuracy were installed. An automatic gas-distribution system was used to deliver gas to the ionization chambers, thus achieving the optimal distribution of He, N₂, Ar, and Kr gases at different energies in the ionization chambers. The automatic gas-inflation function was integrated into the data-acquisition software and operated with a single click.

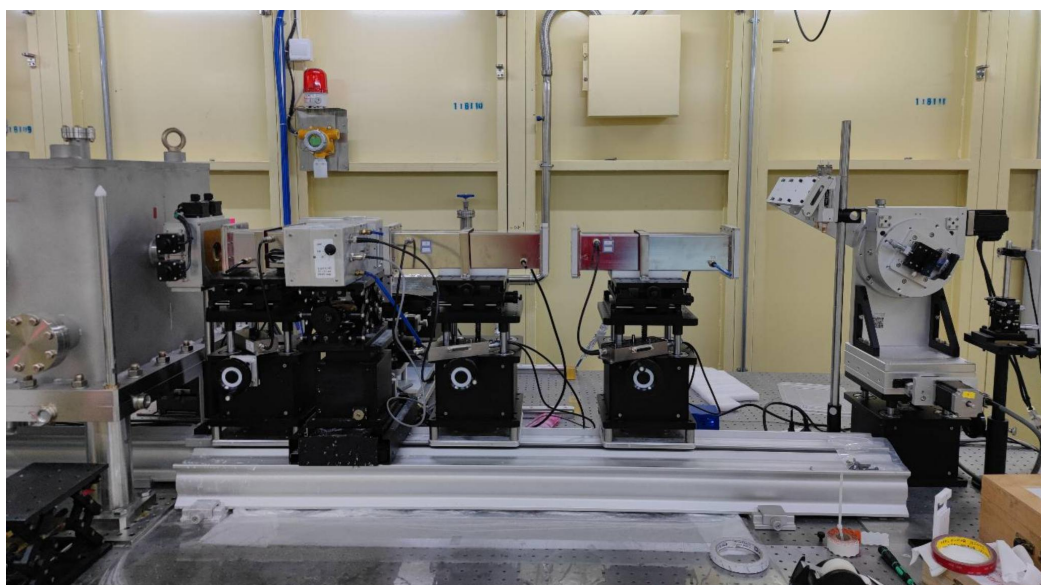


Fig. 5 Schematic diagram of experimental station at BL11B.

3.1 Experimental methods

3.1.1 Transmission-mode XAFS

Transmission measurement is the basic principle of XAFS spectroscopy and is typically performed on concentrated samples (generally > 5 wt%). The setup for this measurement is shown in Fig. 6. Three parallel-plate ionization chambers are set in a straight line and the sample is placed between the first two ionization chambers, whereas a reference foil is placed between the second and third ionization chambers. This layout is useful for monitoring slight shifts in the absorption edges.

Several standard foils have been measured at room temperature in this mode as reference.

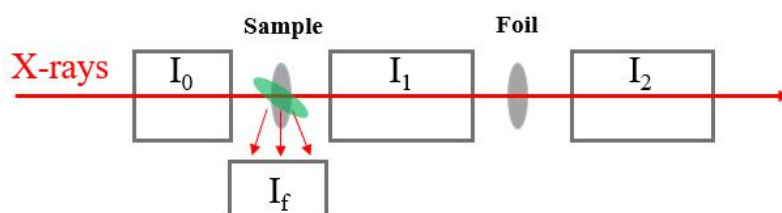


Fig. 6 Arrangement for transmission and fluorescence XAFS measurements. Green region represents fluorescence-sample direction. I_0 , I_1 , I_2 , and I_f indicate X-ray intensities from first, second, and third ionization chambers as well as fluorescence detector, respectively.

Typically, the L_3 edge of the Pt foil is measured at BL11B, as shown in Fig. 7. It exhibits excellent quality with sharp absorption features and a low noise of $k^3\chi(k)$, which extends to high wavenumbers of up to 20 \AA^{-1} (more than 1500 eV above the edge). In most studies, an energy range of 800–1000 eV above the edge is sufficient and allows all EXAFS spectrum data to be measured within 10 min.

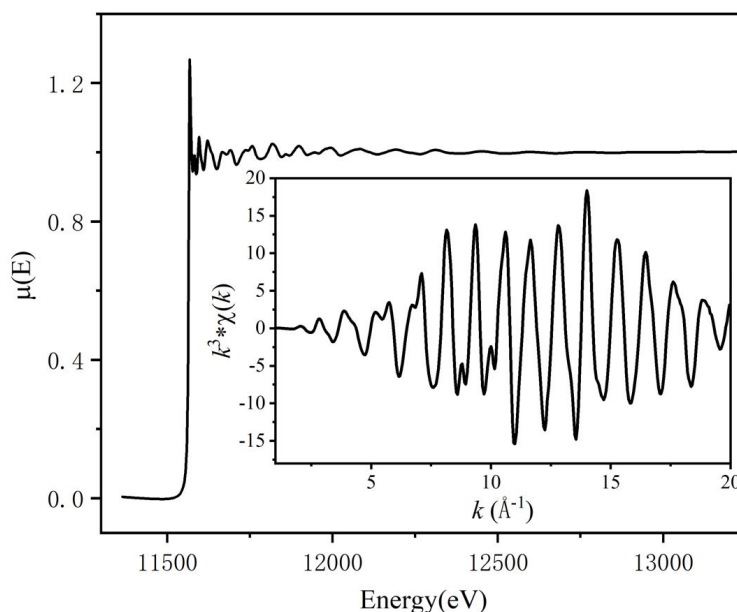


Fig. 7 L_3 -edge absorption spectra of Pt metal foils measured in transmission mode at BL11B; inset shows $k^3\chi(k)$.

3.1.2 Fluorescence-mode XAFS

For samples with low absorbing-element concentrations or those that cannot be penetrated by X-rays, fluorescence measurements are the best option. The layout for such measurements is shown in Fig. 6. A fluorescence detector is placed perpendicular to the beam path on the side of the sample. Four types of detectors for fluorescence measurement are equipped at BL11B. The most commonly used detector is the Lytle-type detector [36], which is an ionization chamber with a large detection area. The second is the PIPS detector (Mirion Technologies, Inc.), whose rapid response enables effective conventional XAFS and QXAFS measurements [37]. These detectors cannot distinguish between X-ray photons of different energies. The other two detectors include a monolithic 36-pixel high-purity germanium detector [38] (Canberra) with XIA FalconX

electronics and a four-element silicon drift detector [39] (SDD, Hitachi Vortex) with Xspress3 electronics. These detectors feature high energy resolution and are optimal for measuring samples of lower concentrations.

Typically, the spectra of a Co_3O_4 sample with a Co concentration of approximately 0.5 wt% is measured at BL11B. As shown in Fig. 8, the normalized spectra and $k^3 \chi(k)$ with different detection modes and detectors are almost identical.

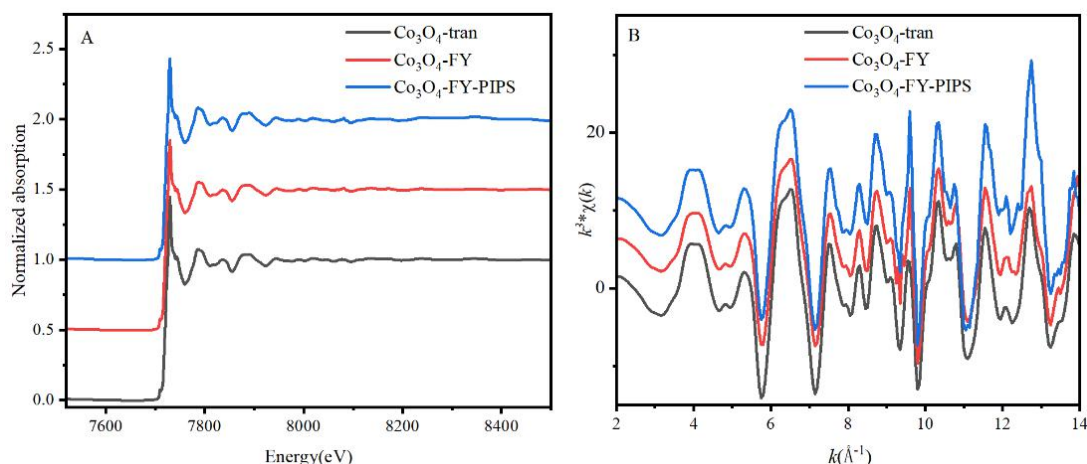


Fig. 8 (A) Comparison of K-edge absorption spectra of Co_3O_4 samples with different detection modes. (B) Comparison of extracted k^3 -weighted EXAFS at Co K-edge of Co_3O_4 . Spectrum of sample with Co concentration greater than 5 wt% is measured in transmission mode (black line, marked Co_3O_4 -tran), whereas spectrum of sample with Co concentration of approximately 0.5 wt% is measured in fluorescence mode using Lytle (red line, Co_3O_4 -FY) and PIPS (blue line, Co_3O_4 -FY-PIPS) detectors, respectively.

For ultralow-concentration or complex systems, the SDD is advantageous for XAFS measurements. For comparison, we measured a sample with 0.5 wt% Pt supported on Fe_2O_3 using Lytle and the SDD, respectively, as shown in Fig. 9. Because of the strong background fluorescence signal of Fe, the signal-to-noise ratio of the spectra acquired by the Lytle detector was unsatisfactory. By contrast, the SDD exhibited a high energy resolution and easily separated the fluorescence signal of Pt from the background. Additionally, the SDD acquired much better data quality, thus demonstrating that it can acquire high-quality absorption spectra of complex systems or ultralow-concentration systems.

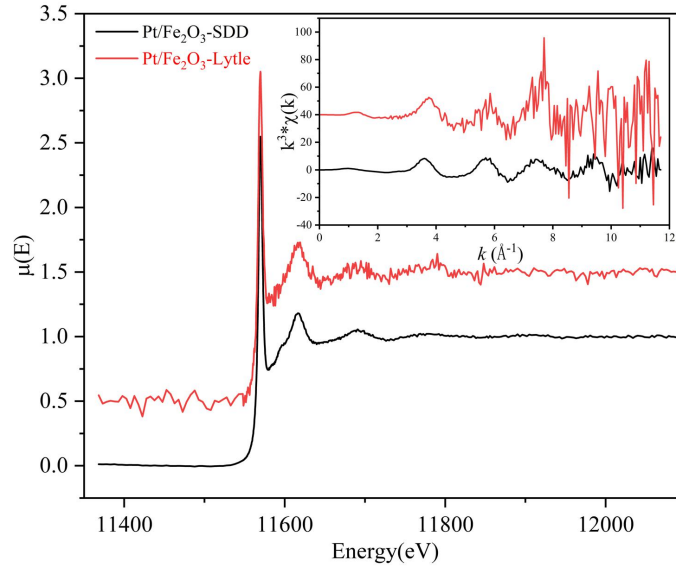


Fig. 9 Comparison of L_3 -edge XAFS of Pt/Fe₂O₃ sample with Pt concentration of approximately 0.5 wt% acquired using SDD and Lytle detector. Inset shows $k^3\chi(k)$.

3.1.3 QXAFS

The time-resolved XAFS technique is effective for investigating dynamic structural changes in materials during physical processes or chemical reactions [40]. The quick-scanning monochromator system is described in Section 2.2.2 and the data-acquisition system is described in Section 3.2. Both the gridded ionization chambers [41] with a fast response time ($< 10 \mu\text{s}$) and the parallel-plate ionization chambers with a slow response time ($\sim 220 \mu\text{s}$) can be used to perform QXAFS measurements within a resolution of 100 ms to 1 s.

The XANES region of the Cu metal foil with an oscillation frequency of 25 Hz was measured. During the acquisition process, the angle encoder values changed over time, as shown in Fig. 10. The measured “up” and “down” spectra were identical, as shown in Fig. 11. The shoulder peak at 8981.3 eV was clearly distinguishable, thus exhibiting high energy resolution.

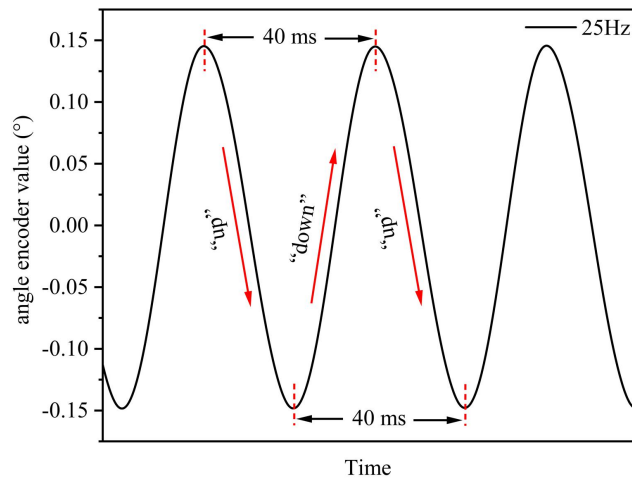


Fig. 10. Angle encoder values based on oscillation frequency of 25 Hz over time. Direction of increasing the energy is defined as “up,” whereas direction of decreasing energy is defined as “down.” A 40 ms cycle period comprises “up” and “down” spectra [42].

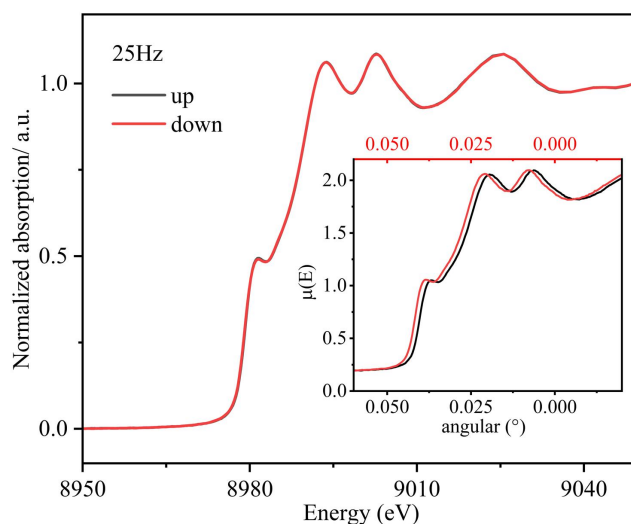


Fig. 11 “Up” and “down” XANES spectra measured at Cu K-edge of Cu metal foil at oscillation frequency of 25 Hz (20 ms per spectrum). Although angular encoder values for “up” and “down” XANES spectra differ, they can be corrected using a standard Cu metal foil.

In addition, the EXAFS spectra of the Cu metal foil with an oscillation frequency of 5 Hz were measured to investigate the capabilities of the fast EXAFS measurements. We compared the k^3 -weighted fine structures of a single 100-ms QXAFS spectrum and the conventional 10-min step-scanning spectra, as shown in Fig. 12. The two EXAFS spectra exhibited comparable results. Although the QXAFS spectrum exhibited minimal noise in the high- k region, the data quality was sufficient for precise structure analysis. These results show that BL11B can perform time-resolved XAFS measurements on a millisecond scale.

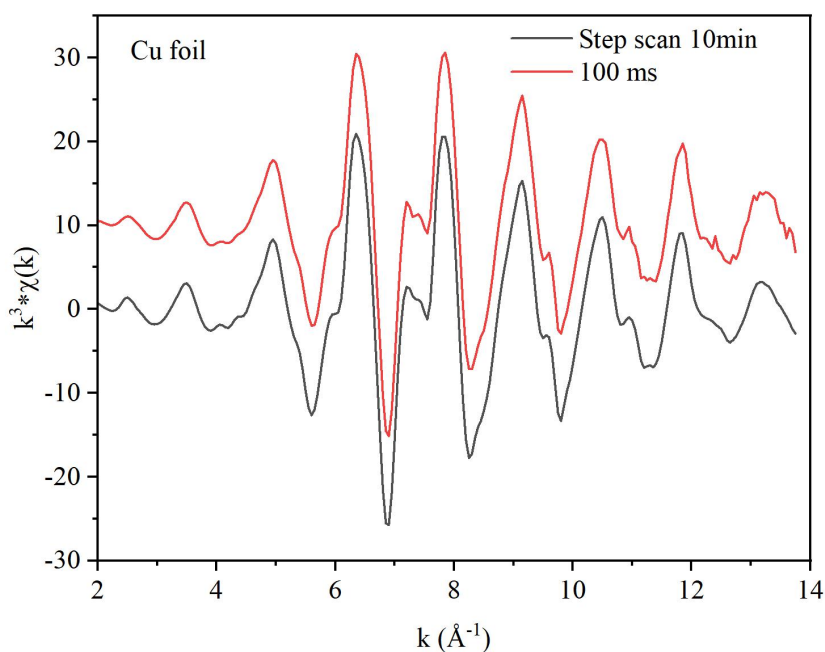


Fig. 12 Extracted k^3 -weighted EXAFS at Cu K-edge of Cu metal foil at quick-scanning mode in 100 ms (red) and step-scanning mode in 10 min (black).

3.1.4 *In situ* XASF sample environments

To facilitate *in situ* XAFS experiments at BL11B, various *in situ* cells have been developed, as shown in Fig. 13. They include A) a high-temperature *in situ* cell, B) an electrochemical *in situ* cell, and C) an ion battery *in-situ* cell.

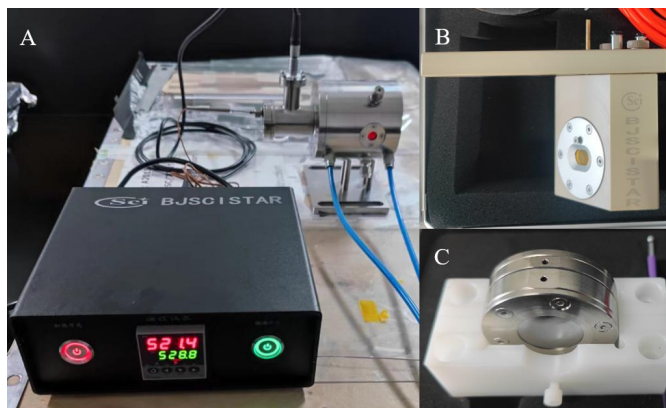


Fig. 13 Various XAFS *in situ* cells

3.2 Beamline control and data-acquisition system

The control system for all the beamline stations at the SSRF uses the Experimental Physics and Industrial Control System (EPICS), which is a widely used distributed control system worldwide. All components in BL11B were controlled using control software based on the EPICS.

The motion control system of BL11B comprises an upper-layer operator interface (OPI), an input/output controller (IOC), and a local area network that connects the OPI and IOC. It uses Control System Studio, which is an Eclipse-based set of tools developed by DESY, SNS, and BNL, to design the control and display the interface of the system.

The data acquisition [43,44] in BL11B was compiled using the QT software, which is an across-platform C++ GUI application-development framework that can be combined with the Python scripting software. It is an easily controllable model for different types of hardware and features a user-friendly graphical interface. It integrates several functions, such as automatic gas distribution, monochromator control, harmonics-rejection mirror control, detector control, and data acquisition, thus significantly improving the efficiency and reliability of XAFS measurements. Fig. 14 shows a schematic illustration of the XAFS measurement system.

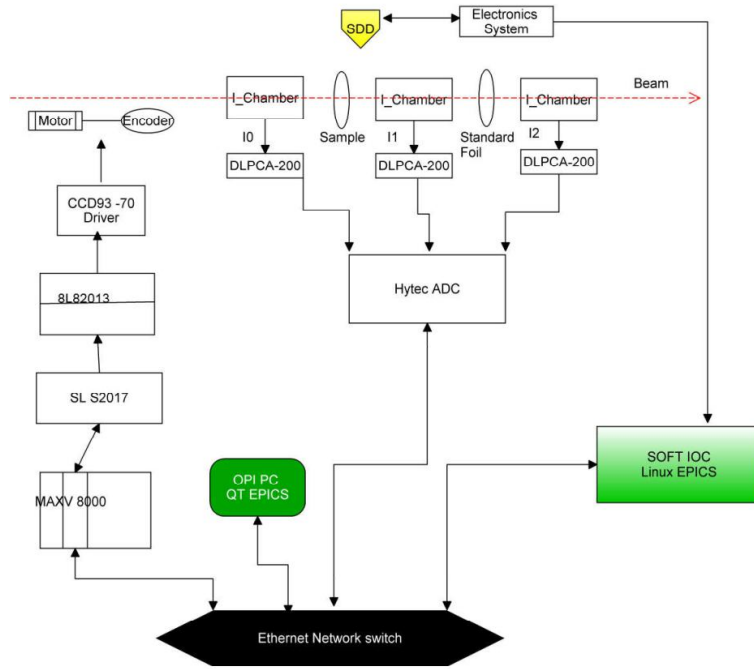


Fig. 14 Schematic layout of data-acquisition system at BL11B.

4 Beamline performance

After the installation of the optical equipment and the distribution of the control system were completed, the beamline was commissioned. The acceptance of the BL11B beamline was conducted in December 2019. The detailed commissioning results are summarized in the following subsections.

4.1 Energy resolution

Energy resolution is the most important parameter for a spectroscopy beamline and depends on all the optical components of the beamline [45]. An energy-resolution measurement system was constructed at the BL11B experimental end-station. The system comprises a Si(111) analyzer crystal, a high-precision rotating stage, a Si PIN photodiode, and software for motion control and data acquisition. A schematic illustration of the measurement process is shown in Fig. 15. The X-rays passing through the sample and ionization chambers hit the downstream analyzer crystal and are diffracted into the Si PIN photodiode. Subsequently, the photodiode records the X-ray intensity as a function of the analyzer crystal's Bragg angle [46].

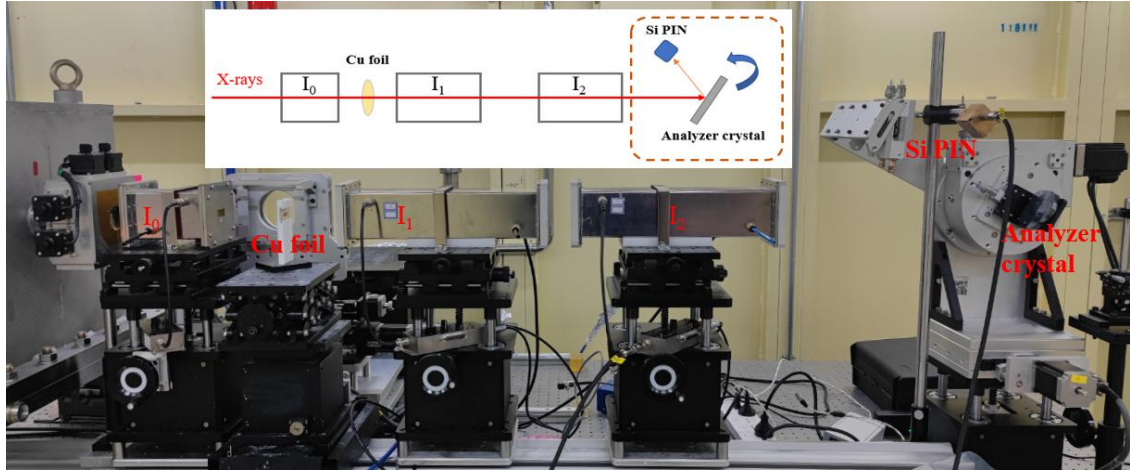


Fig. 15 Energy-resolution measurement device, whose schematic illustration is shown in dotted brown box in inset. Si PIN photodiode is encapsulated in copper shell with aluminized paper window. Intensity of diffracted X-rays is sensitive to angle of analyzer crystal due to its narrow Darwin width.

The energy resolution of the beamline is sensitive to the divergence of the incoming beam in the DCM crystal, which depends on the bending radius of the cylindrical collimating mirror. Therefore, the radius of the collimating mirror was optimized meticulously. First, we set the analyzer crystal to approximately 61.71° relative to the incident beam, which corresponds to the Bragg angle of Si(444) at 8981.3 eV. A series of different bending radii of the collimating mirror was obtained using the stepper motor. For each bending radius, we scanned the DCM from 8960 to 8990 eV and obtained I_0 , I_t , and $I_{Si\ PIN}$ values simultaneously. The XANES spectra of the Cu K-edge and the diffraction curves of the analyzer crystal with different bending radii were obtained, as shown in Fig. 16. Clearly, the height and width of the diffraction curves varied with the bending radius of the collimating mirror. When the bending radius approached the theoretical optimum, the diffraction curve exhibited the highest amplitude and the minimum full width at half maximum (FWHM), as indicated by the black line in Fig. 16A. In other words, the optimal bending radius that resulted in the highest energy resolution for the beamline was obtained. Meanwhile, the sharpest shoulder peak appeared at 8981.3 eV in the Cu K-edge XANES spectrum, as shown in Fig. 16B. This indicates that the energy resolution of BL11B satisfies the requirements of XAFS measurements.

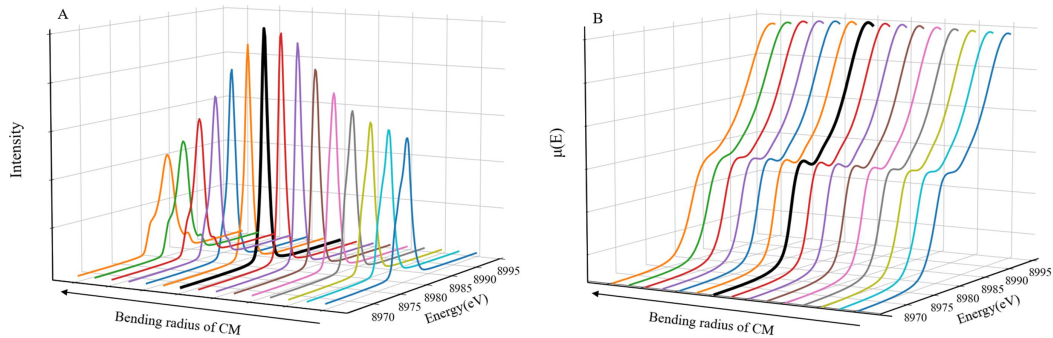


Fig. 16 Diffraction curves (A) and XANES spectra (B) measured simultaneously. Different

bending radii of collimating mirror (CM) are adjusted by stepper motor. (A) As bending radius deviates from theoretical value, diffraction spectra widen gradually, and vice versa. Based on Gaussian fitting and calculations, black line exhibits the minimum FWHM, which corresponds to the optimal bending radius. (B) Shoulder peak of Cu K-edge at 8981.3 eV in XANES spectra becomes sharper as bending radius approaches theoretical value.

Subsequently, the beamline energy resolution was tested quantitatively. The analyzer crystal was set to approximately 81.32° relative to the incident beam, which was approximately the Bragg angle of Si(555) at 10,000 eV. We measured the rocking curve of the analyzer crystal by obtaining the $I_{Si\ PIN}$ while scanning the Bragg angle at the optimal bending radius of the collimating mirror. The rocking curve for Si(555) is shown in Fig. 17. The energy resolution can be expressed as $\Delta E/E = \Delta\theta \times \cot\theta_B$, where θ_B is the Bragg angle of Si(555) at 10 keV, which is 81.32° theoretically, and $\Delta\theta$ is the FWHM of the rocking curve, which is 176.5 arcsec in this study. The total resolution is primarily reflected by the convolution of the beamline energy resolution, the effect of X-ray divergence, and the Darwin width of the crystal analyzer. Based on calculations, the energy resolution of the BL11B beamline exceeds 1.31×10^{-4} at 10 keV for Si(111) of the DCM.

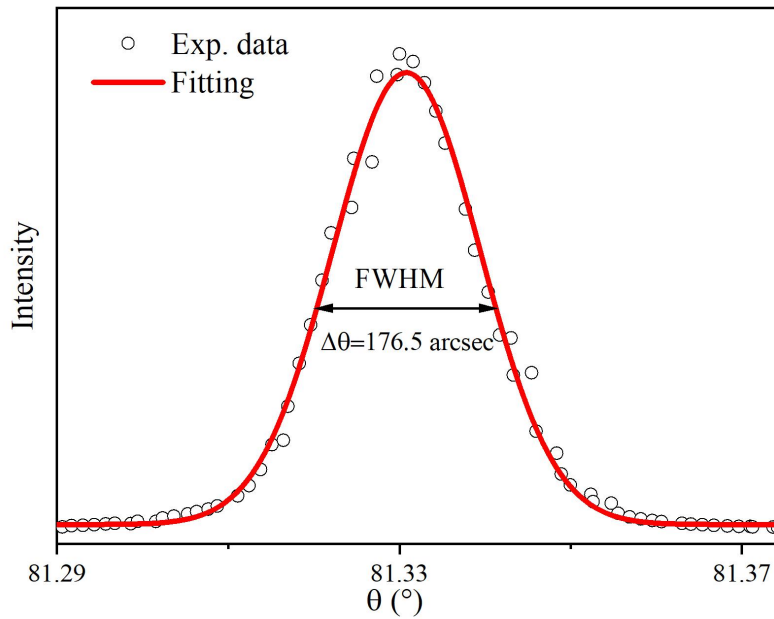


Fig. 17 Rocking curve of Si(555) at optimal bending of collimating mirror. FWHM is 176.5 arcsec based on Gaussian Fitting.

4.2 Photon flux

Using the DCM of the Si(111) crystal, the photon flux at 10 keV was measured using a parallel-plate ionization chamber. The chamber was 15 cm long and filled with pure N_2 gas at atmospheric pressure. The gain of the DLPCA-200 current amplifier used was 10^6 V/A . Using the Hephaestus software, the actual photon flux was calculated to be $4.98 \times 10^{11} \text{ photons/s}$ [47].

4.3 Spot size

The beam-spot shape was displayed in real time using an X-ray imaging detector (X-ray FDS

6.02MP, PSEL) placed at the sample position. The detector was a SCMOS camera with a scintillator (Gadox: Tb) coupled through a fiber-optic input. Its pixel size was $4.54 \mu\text{m} \times 4.54 \mu\text{m}$, which was sufficient for the precise commission of the beamline optics. The spot size was measured by scanning the four-blade slits at the sample position in the vertical and horizontal directions. A parallel-plate ionization chamber was placed behind the four-blade slits, which recorded the X-ray intensity during scanning. Vertical and horizontal spot sizes were obtained by fitting the first derivative of the X-ray intensity. Fig. 18 shows that the FWHM focused spot size was $214 \mu\text{m}$ (H) \times $244 \mu\text{m}$ (V).

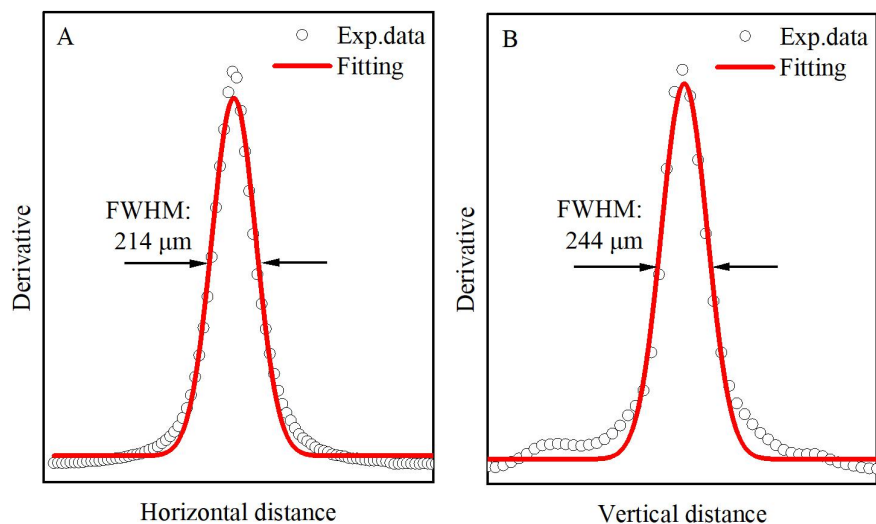


Fig. 18 Focused spot size at sample position. (A) Horizontal and (B) vertical beam-spot profiles. FWHMs obtained via Gaussian fitting.

4.4 Stability

To verify the performance and stability of the beamline, continuous EXAFS was performed on the Cu metal foil for more than 130 times over 20 h, as shown in Fig. 19. All the spectra in both the E- and k-spaces were almost identical without a noticeable energy shift, thus demonstrating the excellent long-term stability and capacity of the beamline for continuous measurements over a long duration.

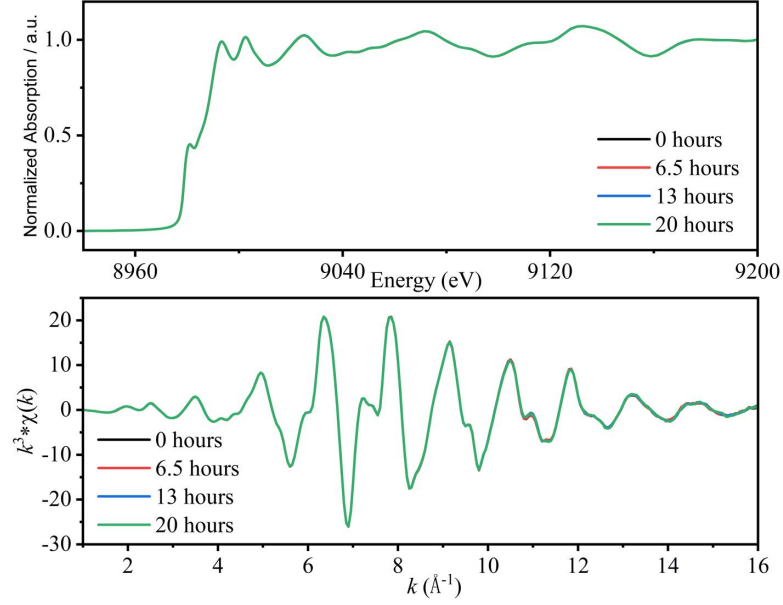


Fig. 19 Comparisons of XANES of Cu metal foil in continuous cycle. All spectra in E-and k-spaces are coincident without energy shift.

The static beam positions on the sample were monitored using a quadrant beam position monitor when using the DCM. Assuming that the change in the beam position in the horizontal direction was much smaller than that in the vertical direction, we focused on the vertical position stability over time, as shown in Fig. 20. The standard deviation was approximately $0.27 \mu\text{m}$, which demonstrates favorable stability at the beam position.

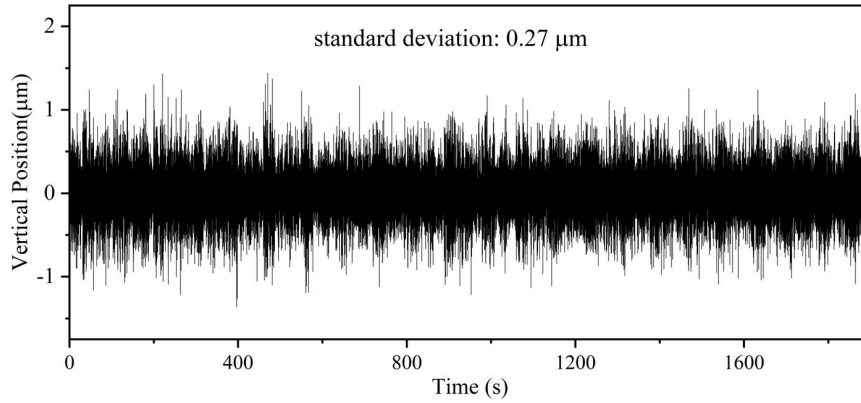


Fig. 20. Vertical position of beamline spot with time. Effects of low-frequency oscillations and electron-beam slow drifts are removed via high-pass filtering.

4.4 Experimental results

The overall performance of BL11B was first demonstrated by measuring the K-edge XAFS spectrum of the Cu metal foil in transmission mode, as shown in Fig. 21. Both the XANES spectrum with a clear shoulder peak and the k^3 -weighted EXAFS spectrum up to 18 \AA^{-1} confirmed the high performance of BL11B.

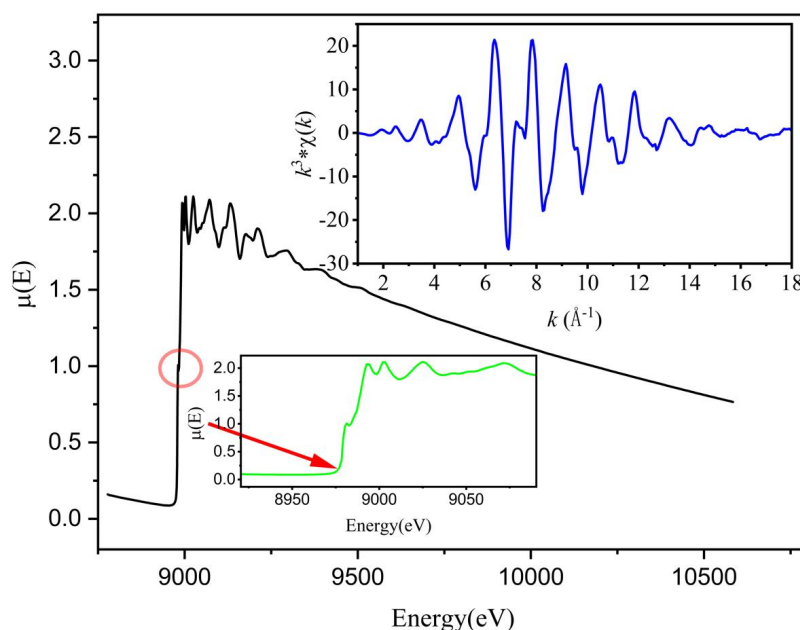


Fig. 21 K-edge XAFS of Cu metal foil. Green line in lower inset indicates XANES feature, and blue line in upper inset indicates k^3 -weighted EXAFS in k -space.

5 Summary and conclusion

The BL11B beamline at the SSRF is dedicated to conventional and millisecond-scale QXAFS spectroscopy. The beamline is currently in operation and has been available for general user proposals since January 2021. The BL11B beamline offers a wide energy range (i.e., 5–30 keV), a submillimeter-focused spot size, high energy resolution and stability, and various types of *in situ* experimental equipment. Various experimental techniques have been developed, including transmission XAFS, fluorescence XAFS, QXAFS, and *in situ* XAFS. Consequently, more than 300 papers have been published in various scientific fields, thus demonstrating the excellent performance of the beamline. Meanwhile, new experimental techniques are being devised, including the combination of XAFS, XRD, and high-energy-resolution XAFS, which are expected to be operable by the general user community in the future. In conclusion, the BL11B beamline is an effective research platform for the fields of energy materials, catalysis, environmental science, and condensed matter physics. Furthermore, the beamline is advantageous to industrial application studies.

Acknowledgments

The authors are grateful for the continued assistance and collaboration of the support groups at the SSRF (hardware controls and data acquisition, engineering design and installation, alignment, electronics, and safety interlocking).

Author contributions:

All authors contributed to the study conception and design. Material preparation, data collection and analysis were performed by Jiong Li and Yu Chen. The first draft of the manuscript was written by Yu Chen and all authors commented on previous versions of the manuscript. All authors read and approved the final manuscript.

Data Availability Statement:

The data that support the findings of this study are openly available in Science Data Bank at <https://cstr.cn/31253.11.sciencedb.j00186.00057> and <https://www.doi.org/10.57760/sciencedb.j00186.00057>.

References

1. P.A. Lee, P.H. Citrin, P. Eisenberger et al., Extended x-ray absorption fine structure—its strengths and limitations as a structural tool. *Rev. Mod. Phys.* **53**, 769-806 (1981). doi:10.1103/revmodphys.53.769.
2. Bunker G, Introduction to XAFS: A Practical Guide to X-Ray Absorption Fine Structure Spectroscopy. Cambridge: Cambridge University Press (2010). doi:10.1017/CBO9780511809194
3. J.D. Grunwaldt, B. Kimmeler, A. Baiker et al., Catalysts at work: From integral to spatially resolved X-ray absorption spectroscopy. *Catal.* **145**, 267-278 (2009). doi:10.1016/j.cattod.2008.11.002
4. Q. Fu, W.X. Li, Y.X. Yao et al., Interface-confined ferrous centers for catalytic oxidation. *Science* **328**, 1141-1144 (2010). doi:10.1126/science.1188267
5. B.T. Qiao, A.Q. Wang, X.F. Yang et al., Single-atom catalysis of CO oxidation using Pt₁/FeO_x. *Nat. Chem.* **3**, 634-641 (2011). doi:10.1038/nchem.1095
6. S. Bordiga, E. Groppo, G. Agostini et al., Reactivity of surface species in heterogeneous catalysts probed by in situ X-ray absorption techniques. *Chem. Rev.* **113**, 1736-1850 (2013). doi:10.1021/cr2000898
7. Z.H. Sun, Q.H. Liu, T. Yao et al., X-ray absorption fine structure spectroscopy in nanomaterials. *Sci. China Mater.* **58**, 313-341 (2015). doi:10.1007/s40843-015-0043-4
8. S. Zhang, S.Q. Gu, Y. Wang et al., Spontaneous Delithiation under Operando Condition Triggers Formation of an Amorphous Active Layer in Spinel Cobalt Oxides Electrocatalyst toward Oxygen Evolution. *ACS Catal.* **9**, 15195-15195 (2019). doi:10.1021/acscatal.9b00928.
9. W.D. Cheng, M.Y. Zhao, Y.C. Lai et al., Recent advances in battery characterization using in situ XAFS, SAXS, XRD, and their combining techniques: From single scale to multiscale structure detection. *Exploration* **4**, 20230056 (2024). doi:10.1002/EXP.20230056
10. H.N. Sun, W. Zhou, Progress on X-ray Absorption Spectroscopy for the Characterisation of Perovskite-Type Oxide Electrocatalysts. *Energ. Fuel.* **35**, 5716-5737 (2021). doi:10.1021/acs.energyfuels.1c00534
11. X. Liang, N.H. Fu, S.C. Yao et al., The Progress and Outlook of Metal Single-Atom-Site Catalysis. *J. Am. Chem. Soc.* **144**, 40 (2022). doi: 10.1021/jacs.1c12642

12. P.P. Du, R. Si, Z.S. Li et al., Applications of X-ray Absorption Fine Structure Spectroscopy in the Photocatalytic Conversion of Small Molecules. *ACS Catal.* **13**, 6690–6703 (2023). doi:10.1021/acscatal.2c06413
13. T. Gan, D.S. Wang, Atomically dispersed materials: Ideal catalysts in atomic era. *Nano Res.* **17**, 18–38 (2024). doi:10.1007/s12274-023-5700-4
14. A.D. Handoko, F. Wei, Jenndy et al., Understanding heterogeneous electrocatalytic carbon dioxide reduction through operando techniques. *Nat. Catal.* **1**, 922–934 (2018). doi: 10.1038/s41929-018-0182-6
15. A. Bergmann, B. Roldan Cuenya, Operando insights into nanoparticle transformations during catalysis. *ACS Catal.* **9**, 10020-10043 (2019). doi:10.1021/acscatal.9b01831
16. J. Zhou, Y. Wang, X.Z. Su et al., Electrochemically accessing ultrathin Co (oxy)-hydroxide nanosheets and operando identifying their active phase for the oxygen evolution reaction. *Energy Environ. Sci.* **12**, 739-746 (2019). DOI:10.1039/C8EE03208D.
17. C.Y. Yang, X.X. Zhang, Q.Z. An et al., Dynamically-evolved surface heterojunction in iridium nanocrystals boosting acidic oxygen evolution and overall water splitting. *J. Energy Chem.* **78**, 374-380 (2023). doi:10.1016/j.jechem.2022.12.032.
18. D. Friebe, M.W. Louie, M. Bajdich et al., Identification of highly active Fe sites in (Ni,Fe)OOH for electrocatalytic water splitting. *J. Am. Chem. Soc.* **137**, 1305-1313 (2015). doi:10.1021/ja511559d
19. R. Zhang, L. Pan, B. Guo et al., Tracking the role of defect types in Co₃O₄ structural evolution and active motifs during oxygen evolution reaction. *J. Am. Chem. Soc.* **145**, 2271-2281 (2023). doi:10.1021/jacs.2c10515
20. H. Su, W.L. Zhou, W. Zhou et al., In-situ spectroscopic observation of dynamic-coupling oxygen on atomically dispersed iridium electrocatalyst for acidic water oxidation. *Nat. Commun.* **12**, 6118 (2021). doi:10.1038/s41467-021-26416-3
21. Q.B. Wu, J.W. Liang, M. J. Xiao et al., Non-covalent ligand-oxide interaction promotes oxygen evolution. *Nat. Commun.* **14**, 997 (2023). doi:10.1038/s41467-023-36718-3
22. J.Y. Duan, T.Y. Liu, Y.H. Zhao et al., Active and conductive layer stacked superlattices for highly selective CO₂ electroreduction. *Nat. Commun.* **13**, 2039 (2022). doi:10.1038/s41467-022-29699-2
23. S. F. Ji, B. Jiang, H.G. Hao et al., Matching the kinetics of natural enzymes with a single-atom iron nanozyme. *Nat. Catal.* **4**, 407–417 (2021). doi:10.1038/s41929-021-00609-x
24. M.Y. Wang, L. Árnadóttir, Z. C. J. Xu et al., In Situ X-ray Absorption Spectroscopy Studies of Nanoscale Electrocatalysts. *Nano-Micro Lett.* **11**, 47 (2019). doi:10.1007/s40820-019-0277-x
25. Y.N. Xie, T.D. Hu, T. Liu et al., The 1W1B-XAFS Beam Line at BSRF. *AIP Conf. Proc.* **879**, 856–859 (2007). doi:10.1063/1.2436195
26. H.S. Yu, X.J. Wei, J. Li et al., The XAFS beamline of SSRF. *Nucl. Sci. Tech.* **26**, 6–12 (2015). doi:10.13538/j.1001-8042/nst.26.050102
27. O. Müller, M. Nachtegaal, J. Just et al., Quick-EXAFS setup at the SuperXAS beamline for in situ X-ray absorption spectroscopy with 10 ms time resolution. *J. Synchrotron Rad.* **23**, 260-266 (2016). doi:10.1107/S1600577515018007
28. V. Briois, C. L. Fontaine, S. Belin et al., ROCK: the new Quick-EXAFS beamline at SOLEIL. *J. Phys.: Conf. Ser.* **712**, 012149 (2016). doi:10.1088/1742-6596/712/1/012149

29. B. Bornmann, J. Kläs, O. Müller., The quick EXAFS setup at beamline P64 at PETRA III for up to 200 spectra per second. *AIP Conf. Proc.* **2054**, 040008 (2019). doi:10.1063/1.5084609
30. C.W. Pao, J.L. Chen, J.F. Lee et al., The new X-ray absorption fine-structure beamline with sub-second time resolution at the Taiwan Photon Source. *J. Synchrotron Rad.* **28**, 930-938 (2021). doi:10.1107/S1600577521001740
31. Z.T. Zhao, H.J. Xu, H. Ding, Status of the Shanghai Synchrotron Radiation Facility. *IEEE. Part. Acc. Conf.* 214-216 (2005). doi:10.1109/PAC.2005.1590398
32. M.H. Jiang, X. Yang, H.J. Xu et al., Shanghai synchrotron radiation facility. *Chin. Sci. Bull.* **54**, 4171-4181 (2009). doi:10.1007/s11434-009-0689-y
33. Rebuffi L, Sánchez del Río M. ShadowOui: a new visual environment for X-ray optics and synchrotron beamline simulations. *J. Synchrotron Rad.* **23**, 1357-1367 (2016). doi:10.1107/S1600577516013837
34. J.H. He, Z.T. Zhao, Shanghai synchrotron radiation facility. *Natl. Sci. Rew.* **1**, 171 (2014). <https://doi.org/10.1093/nsr/nwt039>
35. H.J. Xu, T.Q. Xiao, Shanghai Synchrotron Radiation Facility Project Review and Its Current Status(in Chinese). *Journal of Fudan University.* **62**, 310-321 (2023). doi:10.15943/j.cnki.fdxh-jns.2023.03.002
36. F.W. Lytle, R.B. Gregor, D.R. Sandstrom et al., Measurement of soft X-ray absorption spectra with a fluorescent ion chamber detector. *Nucl. Instrum. Methods. Phys. Res. A.* **226**, 542-548 (1984). doi:10.1016/0168-9002(84)90077-9
37. A.H. Clark, P. Steiger, B. Bornmann et al., Fluorescence-detected quick-scanning X-ray absorption spectroscopy. *J Synchrotron Rad.* **27**, 681-688 (2020). doi:10.1107/S1600577520002350
38. H. Oyanagi, M. Martini, M. Saito, Nineteen-element high-purity Ge solid-state detector array for fluorescence X-ray absorption fine structure studies. *Nucl. Instrum. Methods Phys. Res. A,* **403**, 58-64 (1998). doi:10.1016/S0168-9002(97)00927-3
39. L. Strüder, P. Lechner, P. Leutenegger, Silicon drift detector – the key to new experiments. *Sci. Nat.* **85**, 539–543 (1998). doi:10.1007/s001140050545
40. Y. Iwasawa, K. Asakura, M. Tada, XAFS techniques for catalysts, nanomaterials, and surfaces. Cham: Springer International Publishing, 93- 108 (2017). doi:10.1007/978-3-319-43866-5
41. O. Müller, J. Stötzel, D. Lützenkirchen-Hecht et al., Gridded ionization chambers for time resolved X-ray absorption spectroscopy. *J. Phys.: Conf. Ser.* **425**, 092010 (2013). doi:10.1088/1742-6596/425/9/092010
42. O. Müller, D. Lützenkirchen-Hecht, R. Frahm, Quick scanning monochromator for millisecond in situ and in operando X-ray absorption spectroscopy. *Rev. Sci. Instrum.* **86**, 093905 (2015). doi:10.1063/1.4929866
43. Y. Zou, S.Q. Gu, Z. Jiang et al., Data acquisition system of XAFS beamline experimental station based on Labview(in Chinese). *Nucl. Tech.* **32**, 5 (2009). doi: 10.3321/j.issn:0253-3219.2009.04.002
44. R.Y. Lu, Q. Gao, S.Q. Gu et al., Data-collection system for high-throughput X-ray absorption fine structure measurements. *Nucl. Sci. Tech.* **27**, 82 (2016). doi:10.1007/s41365-016-0084-8
45. S. Mobilio, F. Boscherini, C. Meneghini, Synchrotron Radiation: Basics, Methods and Applications. Springer-Verlag, Berlin. (2015). doi: 10.1007/978-3-642-55315-8

46. C. Li, M.T. Liu, Z.Y. Zhang et al., Method for energy bandwidth measurement of synchrotron radiation focused beam. *Acta Opt. Sin.* **40**, 1934001 (2020). doi:10.3788/AOS202040.1934001
47. B. Ravel, M. Newville, ATHENA, ARTEMIS, HEPHAESTUS: data analysis for X-ray absorption spectroscopy using IFEFFIT. *J Synchrotron Radiat.* **12**, 537-541 (2005). doi:10.1107/S0909049505012719